Artificial versus Natural Crystals: Effective Wave Impedance of Printed Photonic Bandgap Materials

Chryssoula A. Kyriazidou, *Member, IEEE,* Harry F. Contopanagos, *Member, IEEE,* William M. Merrill, *Student Member, IEEE,* and Nicólaos G. Alexópoulos, *Fellow, IEEE*

***Abstract*—Printed metallo-dielectric photonic bandgap (PBG) materials are analyzed using an analytical approach based on multipole expansions for the scattered fields off individual scatterers and a transfer-matrix method for reconstructing the total scattered fields created by successive lattice planes of the artificial crystal. An effective description of the PBG medium is derived and its correspondence with *natural* crystals is further advanced through an analysis based on Lorentzian response functions, which characterize natural crystals. The effective wave impedance and bulk reflection coefficient of the medium are provided and their properties inside and outside the bandgaps are examined. The presented treatment for these effective response functions extends far beyond the traditional effective medium theory (EMT) limits.**

***Index Terms*—Artificial crystals, frequency selective surfaces, photonic bandgap materials, synthetic materials, synthetic substrates.**

I. Introduction

IN RECENT years, photonic bandgap (PBG) materials [1]–[3] have attracted a lot of attention in the engineering community because they are naturally suited for a variety of antenna gain enhancement and radiation pattern shaping applications [4]–[7], filtering applications (including frequency selective surfaces and space filters), high Q structures [8], integrated circuits, and printed antenna substrates/superstrates where filtering response of particular modes (e.g., surface modes) is desired, as well as for the analysis and design of absorbing thin film structures [9].

These materials are composed of unit cells containing artificial implants embedded within a host dielectric and periodically placed to form an artificial crystal lattice in one, two, or three dimensions. The scattering response of the implants is intended to be very different than the surrounding dielectric host, creating significant electromagnetic interference between implant and host. This interference depends on both host and implant (design of unit cell) and crystal geometry. By appropriate design of these parameters, one can achieve large transmission suppressions in specific frequency bands (PBG) and uninhibited transmission in other bands.

Up until now, the most interesting characteristics of these materials, namely their frequency response near the bandgaps, have been explored primarily by numerical methods. These are typically finite-difference time-domain (FDTD) codes [10]–[12] and hybrids of finite elements and method of moments codes [13]–[16], or approaches based on the layer-Korringa–Kohn–Rostoker (KKR) method [17] and on a plane wave expansion [18], [19]. Despite the fact that these codes can handle a variety of device-specific applications incorporating such materials as well as provide dispersion diagrams for the materials themselves, the physical details of electromagnetic propagation and scattering in these materials remains untransparent, to say the least. This is especially true for device-specific applications, where complicated excitations and radiation properties of the primary device components make any clear separation of the material properties almost impossible.

A second disadvantage of a purely numerical case-by-case approach to these composite materials is the very long processing time these codes require and the memory requirements imposed on the corresponding machine. This makes any attempt of systematic parameter-space search and electromagnetic optimization of these materials very time consuming, even within a large present-day computing environment.

These two reasons motivate the present development of an analytical approach to a class of metallo-dielectric PBG materials relevant to engineering applications. We focus on a lattice of printed elements immersed into a low-loss host dielectric. This is a class of structures that are easily and inexpensively fabricated and are appropriate for monolithic integration. In Section II, we present a transfer-matrix analysis of such geometries for oblique TE plane wave incidence and derive closed analytical expressions for the reflection and transmission in terms of the shunt susceptance of a planar array of printed elements. The shunt susceptance itself is analytically calculable for a variety of printed shapes [20], but in this paper we consider printed disks. We demonstrate the existence of photonic bandgaps for this structure, for normal incidence and point out that it can operate as a magnetic wall. In Section III, we provide a derivation for the effective wave impedance at normal incidence, which fully describes the bulk reflectivity of the structure. This leads us to establishing a correspondence between this type of artificial (photonic) crystals and natural (atomic) crystals. We find

Manuscript received May 28, 1998; revised February 11, 1999. This work was supported in part by the U.S. Army Research Office under Contract DAAH04-96-1-0389.

C. A. Kyriazidou and W. M. Merrill are with the Department of Electrical Engineering, University of California Los Angeles, Los Angeles, CA 90095 USA (e-mail: {kyria; williamm}@ucla.edu).

H. F. Contopanagos was with the Department of Electrical Engineering, University of California Los Angeles, Los Angeles, CA 90095 USA. He is now with HRL Laboratories, Malibu, CA 90265 USA.

N. G. Alexópoulos is with the Department of Electrical and Computer Engineering, University of California Irvine, Irvine, CA 92697 USA (e-mail: alfios@uci.edu).

Publisher Item Identifier S 0018-926X(00)02622-3.

that these artificial media can be described by Lorentzian resonances, much like the natural crystals in their quantum-mechanical interaction with the electromagnetic field.

We stress that our approach extends far beyond the validity regime of standard effective medium theories (EMT's). The latter are valid for wavelengths typically ten times longer than the characteristic electrical dimensions of the unit cell and, *almost by definition*, cannot provide any information on the behavior near the first bandgap. Instead, our approach is valid typically for unit cell dimensions of the order of the free-space wavelength and it will be shown that this regime typically includes several bandgaps.

II. Transfer-Matrix Analysis of Printed PGB Materials

We consider an orthogonal lattice of PEC disks embedded in a homogeneous dielectric of complex relative permittivity $\epsilon_d \equiv \epsilon_d^r - j\epsilon_d^i$ and thickness c, as shown in Fig. 1. The material will be made by stacking an arbitrary number N of such planar arrays and will be laterally infinite, but of a finite arbitrary thickness $w = Nc$. We present closed analytical formulas for the reflection and transmission coefficients of this material under TE oblique plane wave incidence.

Consider the slab made up by stacking N layers of the corresponding two-dimensional (2-D) PBG medium and excited by TE plane wave oblique incidence at angle θ. Using standard transfer matrix theory [21], we obtain for the transmission coefficient

$$\Gamma_N \equiv \frac{L_0}{R_0} = \frac{S_{21}}{S_{11}}$$
$$T_N \equiv \frac{R_{\text{out}}}{R_0} = \frac{1}{S_{11}}, \qquad \text{with } \begin{pmatrix} R_0 \\ L_0 \end{pmatrix} = S \begin{pmatrix} R_{\text{out}} \\ 0 \end{pmatrix} \quad (1)$$

where R_0 (L_0) is the right (left)-going wave amplitude (with respect to the stacking direction z) in the region of incidence and R_{out} the final right-going wave amplitude in the region past the whole structure.

The scattering matrix S is given in terms of the unit-cell transfer matrix U by

$$S = T_{a,d} U^N T_{d,a} \quad (2)$$

where $T_{a,d}$ is the transfer matrix through an air-dielectric interface. The unit-cell matrix, on the other hand, may obviously be written as

$$U = P_{c/2} T_Y P_{c/2} \quad (3)$$

where $P_{c/2}$ is the propagation matrix through a dielectric region of thickness $c/2$ and T_Y is the transfer matrix through a planar array of scatterers considered as a shunt admittance Y for scattering purposes.

On material interfaces the transfer matrices may be calculated by imposing the usual boundary conditions on the $\boldsymbol{E}$ and $\boldsymbol{H}$ fields. On the shunt admittance plane the correct boundary conditions are those of an electric current sheet set up by the voltage impressed by $\boldsymbol{E}$ across the admittance

$$\boldsymbol{n} \times \boldsymbol{E} = \text{continuous},$$

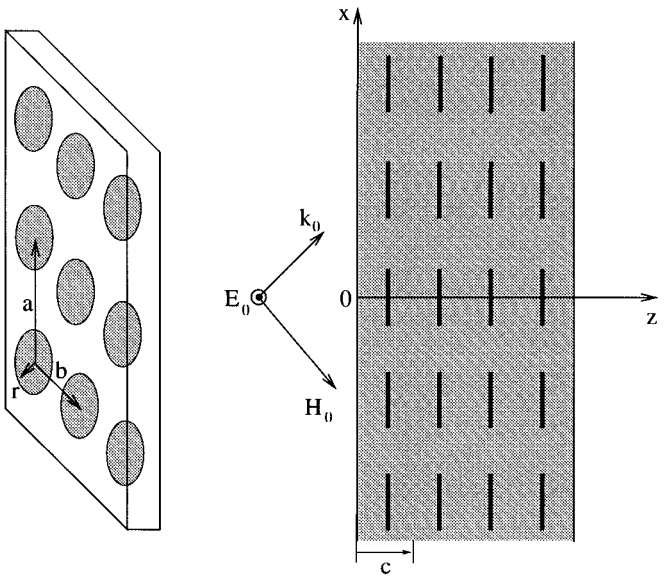

Fig. 1. PBG material made of PEC disks embedded in a dielectric host.

$$\boldsymbol{n} \times [\boldsymbol{H}(z_0^-) - \boldsymbol{H}(z_0^+)] = Y \boldsymbol{E}_{\tan}(z_0) \quad (4)$$

where

- Y is the surface admittance of the 2-D planar array of scatterers embedded within the host dielectric,
- $\boldsymbol{n}$ is the unit normal (along the z-direction in this case), and
- z_0 the position of the admittance plane.

These boundary conditions determine the transfer and propagation matrices as follows:

$$T_{a,d} = \frac{1}{2} \begin{pmatrix} 1 + \dfrac{\overline{\eta}_a}{\overline{\eta}_d} & 1 - \dfrac{\overline{\eta}_a}{\overline{\eta}_d} \\ 1 - \dfrac{\overline{\eta}_a}{\overline{\eta}_d} & 1 + \dfrac{\overline{\eta}_a}{\overline{\eta}_d} \end{pmatrix}$$
$$T_Y = \frac{1}{2} \begin{pmatrix} 2+Y & Y \\ -Y & 2-Y \end{pmatrix}$$
$$P_{c/2} = \begin{pmatrix} e^{\gamma_d c/2} & 0 \\ 0 & e^{-\gamma_d c/2} \end{pmatrix}. \quad (5)$$

Notice that while both kinds of transfer matrices obey their respective group properties $T_{a,d} T_{d,a} = 1 = T_Y T_{-Y}$, the material interface is described by a symmetric matrix, while the shunt admittance interface by an antisymmetric matrix. The unit cell transfer matrix is calculated to be

$$U = \tfrac{1}{2} \begin{pmatrix} e^{\gamma_d c}(2+Y) & Y \\ -Y & e^{-\gamma_d c}(2-Y) \end{pmatrix}. \quad (6)$$

In the above, $\gamma_i, \overline{\eta}_i$ are the oblique propagation constants and relative wave impedances, respectively, for material $i = \{a, d\}$ ($a \equiv$ air, $d \equiv$ dielectric), namely

$$\gamma_i = jk_0 n_i \cos\theta_i, \quad \overline{\eta}_i = \frac{1}{n_i \cos\theta_i}$$
$$\cos\theta_i = \sqrt{1 - \frac{1}{n_i^2} \sin^2\theta}, \quad n_i = \sqrt{\epsilon_i} \quad (7)$$

where $\theta = \theta_a$ is the incidence angle. Using the method outlined above, we calculate the transmission coefficient through the structure to be

$$\begin{aligned} T_N = 4\Bigg\{ & \left(1+\frac{\overline{\eta}_a}{\overline{\eta}_d}\right)\left(1+\frac{\overline{\eta}_d}{\overline{\eta}_a}\right)(U^N)_{11} \\ & + \left(1-\frac{\overline{\eta}_a}{\overline{\eta}_d}\right)\left(1+\frac{\overline{\eta}_d}{\overline{\eta}_a}\right)(U^N)_{21} \\ & + \left(1+\frac{\overline{\eta}_a}{\overline{\eta}_d}\right)\left(1-\frac{\overline{\eta}_d}{\overline{\eta}_a}\right)(U^N)_{12} \\ & + \left(1-\frac{\overline{\eta}_a}{\overline{\eta}_d}\right)\left(1-\frac{\overline{\eta}_d}{\overline{\eta}_a}\right)(U^N)_{22}\Bigg\}^{-1}. \end{aligned} \tag{8}$$

Similarly, the reflection coefficient off the structure is

$$\begin{aligned} \Gamma_N = \frac{1}{4}T_N \times \Bigg\{ & \left(1-\frac{\overline{\eta}_a}{\overline{\eta}_d}\right)\left(1+\frac{\overline{\eta}_d}{\overline{\eta}_a}\right)(U^N)_{11} \\ & + \left(1+\frac{\overline{\eta}_a}{\overline{\eta}_d}\right)\left(1+\frac{\overline{\eta}_d}{\overline{\eta}_a}\right)(U^N)_{21} \\ & + \left(1-\frac{\overline{\eta}_a}{\overline{\eta}_d}\right)\left(1-\frac{\overline{\eta}_d}{\overline{\eta}_a}\right)(U^N)_{12} \\ & + \left(1+\frac{\overline{\eta}_a}{\overline{\eta}_d}\right)\left(1-\frac{\overline{\eta}_d}{\overline{\eta}_a}\right)(U^N)_{22}\Bigg\}. \end{aligned} \tag{9}$$

The matrix U^N has been calculated in closed analytical form in the Appendix. Substituting, we obtain the results

$$T_N = \frac{2}{[(1+\zeta)\tau]^N}\left\{1+\xi^N+\frac{(1-\xi^N)}{2\sqrt{1-\left(\frac{Y}{2\Psi}\right)^2}}\left[\left(\frac{\overline{\eta}_d}{\overline{\eta}_a}+\frac{\overline{\eta}_a}{\overline{\eta}_d}\right)+\left(\frac{\overline{\eta}_a}{\overline{\eta}_d}-\frac{\overline{\eta}_d}{\overline{\eta}_a}\right)\frac{Y}{2\Psi}\right]\right\}^{-1} \tag{10}$$

[see (11) at the bottom of the page], where

$$\begin{aligned} \Psi &\equiv j\sin(k_0 c n_d \cos\theta_d) + \cos(k_0 c n_d \cos\theta_d)(Y/2) \\ \tau &\equiv \cos(k_0 c n_d \cos\theta_d) + \sin(k_0 c n_d \cos\theta_d)(jY/2) \\ \zeta &\equiv \frac{\Psi}{\tau}\sqrt{1-\left(\frac{Y}{2\Psi}\right)^2}, \quad \xi = \frac{1-\zeta}{1+\zeta}. \end{aligned} \tag{12}$$

It is important to notice that the parameter τ above characterizes the corresponding PBG material that is infinite in the z-direction ($\lim\ N = \infty$). This can be shown by evaluating the Floquet propagation constant along the stacking direction through the eigenvalues of the unit cell matrix U:

$$e^{-jk_F c} = \frac{\mathrm{Tr}(U)}{2} - j\sqrt{\mathrm{Det}(U) - \left(\frac{\mathrm{Tr}(U)}{2}\right)^2}. \tag{13}$$

Given that $\mathrm{Det}(U) = 1$, we have

$$\begin{aligned} \cos(k_F c) = \frac{\mathrm{Tr}(U)}{2} &= \cos(k_0 c n_d \cos\theta_d) \\ &+ \sin(k_0 c n_d \cos\theta_d)(jY/2) \equiv \tau. \end{aligned} \tag{14}$$

The bandgaps of the system are given by the inequality $|\tau| > 1$.

One ingredient that has to be supplied in the above formulas in order to obtain predictions is the shunt admittance of a planar array of scatterers. This calculation can be performed at various degrees of difficulty and validity, depending on the order of the multipole expansion taken into account for the scattered field. For the present, we will use (for the thin disk medium) the shunt admittance that has been calculated analytically in [20].

The result is

$$\begin{aligned} Y &\equiv jB = j(B_C - B_L), \\ B_C &= \frac{16}{3}\left(\frac{r}{a}\right)^3 \frac{a}{b}\frac{a}{c}\frac{n_d k_0 c}{\cos\theta_d}\frac{1}{1-\alpha_e C_e} \\ B_L &= \frac{8}{3}\left(\frac{r}{a}\right)^3 \frac{a}{b}\frac{a}{c} n_d k_0 c\left(\frac{1}{\cos\theta_d} - \cos\theta_d\right)\frac{1}{1-\alpha_m C_m}. \end{aligned} \tag{15}$$

The fine structure provided by the electric and magnetic polarizabilities and lattice interaction constants $(\alpha_e C_e, \alpha_m C_m)$ can be readily calculated for a tetragonal lattice

$$\begin{aligned} \alpha_e C_e &= \frac{16}{3}\left(\frac{r}{a}\right)^3\left[\frac{1.2}{\pi}\left(\frac{a}{b}\right)^3 - 8\pi\left(\frac{a}{b}\right)^3 K_0\left(\frac{2\pi a}{b}\right)\right] \\ \alpha_m C_m &= \frac{16}{3}\left(\frac{r}{a}\right)^3\left[\frac{1.2}{2\pi}\left(\frac{a}{b}\right)^3 + \frac{1.2}{2\pi} - 4\pi\left(\frac{a}{b}\right)^3 \right. \\ &\qquad \left. \cdot K_0\left(\frac{2\pi a}{b}\right) - 4\pi K_0\left(\frac{2\pi b}{a}\right)\right] \end{aligned} \tag{16}$$

where K_0 is the modified Bessel function of the second kind. In the rest of this section, for simplicity, we will use a square transverse lattice $a = b, K_0(2\pi) = 0.000\,91$.

The range of validity of these formulas in r/a is derived from a Clausius–Mossotti argument, where the equivalent volume filling fraction should be $(4/3)\pi(r/a)^3 \le 1/3 \rightarrow r/a \le 0.43$.

$$\Gamma_N = \frac{\frac{(1-\xi^N)}{2\sqrt{1-\left(\frac{Y}{2\Psi}\right)^2}}\left[\left(\frac{\overline{\eta}_d}{\overline{\eta}_a}-\frac{\overline{\eta}_a}{\overline{\eta}_d}\right)-\left(\frac{\overline{\eta}_a}{\overline{\eta}_d}+\frac{\overline{\eta}_d}{\overline{\eta}_a}\right)\frac{Y}{2\Psi}\right]}{1+\xi^N+\frac{(1-\xi^N)}{2\sqrt{1-\left(\frac{Y}{2\Psi}\right)^2}}\left[\left(\frac{\overline{\eta}_d}{\overline{\eta}_a}+\frac{\overline{\eta}_a}{\overline{\eta}_d}\right)+\left(\frac{\overline{\eta}_a}{\overline{\eta}_d}-\frac{\overline{\eta}_d}{\overline{\eta}_a}\right)\frac{Y}{2\Psi}\right]} \tag{11}$$

The much more important range of validity in frequency is derived from the requirement that the leading evanescent mode propagating in the longitudinal dimension z have an amplitude that is at least as suppressed as e^{-1}, i.e., $e^{-\Gamma_{nm}c} \leq e^{-1}$. Using [20]

$$\Gamma_{nm} = \left\{ \left(\frac{2\pi n}{a} + k_0 n_d \sin\theta_d \right)^2 + \left(\frac{m\pi}{b} \right)^2 - (k_0 n_d)^2 \right\}^{1/2} \quad n = 0, \pm 1, \cdots, \; m = 0, 1, \cdots \tag{17}$$

we find from the above inequality (setting $a = b$) (18), shown at the bottom of the page, where $n_d \equiv n_d^r - j n_d^i$. The most stringent constraint of (18) arises when the right-hand side is minimum, which always happens for $(n, m, \theta) = (0, 1, 0)$ irrespective of the other parameters. Hence, we derive a conservative range of validity of our analytical treatment

$$k_0 c \leq \frac{1}{n_d^r} \sqrt{\left(\frac{\pi c}{a} \right)^2 - 1}. \tag{19}$$

The present approach, by restricting itself to propagation of the dominant modes only and, therefore, to the range of (19), would not be able to treat certain special cases. For example, the disks being placed on the air-host interface would have to be excluded because higher modes would have to be accounted for between that interface and the adjacent admittance plane.

To validate our formulas, in Fig. 2 we plot the power transmission through an $N = 2$ disk medium for normal plane wave incidence, in the range of validity of our theory provided by (19). We compare with results obtained from a finite element-integral equation method (FE-IEM) approach of [16], where the scatterers are square patches of the same effective aperture whose side d is given by [22]

$$\frac{d}{a} = \left(\frac{32}{3\pi} \right)^{1/3} \frac{r}{a}. \tag{20}$$

We see that within the range of validity of our theory, the agreement is excellent.

From the above equations we can derive the reflection coefficient for a semi-infinite PBG medium, filling up the half-space $z \geq 0$. This is obviously obtained by taking the limit $N \to \infty$ in (11). One can observe numerically, and prove analytically, that, for lossless dielectric host and PEC scatterers, the complex function ξ in (12) has a modulus equal to unity everywhere in frequency, except in the bandgaps. The correct way to obtain the $N \to \infty$ limit, is to introduce a small amount of *physical* loss in either the host dielectric or the scatterers, or both. This loss will not only provide a more accurate physical description of the medium, but will also yield the correct semi-infinite limit. With

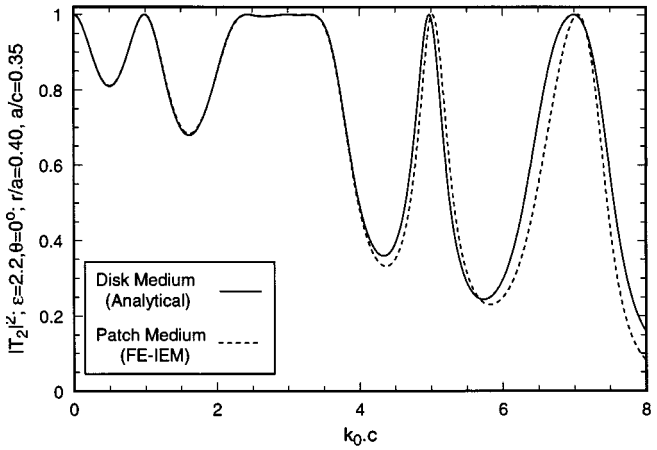

Fig. 2. Comparison between our analytical predictions and the FE-IEM code of [16] for normal plane-wave incidence.

the host permittivity containing any amount of loss, it follows that $|\xi| < 1$ anywhere. Therefore, from (11) we obtain

$$\Gamma_\infty \equiv \lim_{N\to\infty} \Gamma_N = \frac{\dfrac{1}{2\sqrt{1-p^2}} \left[\left(\dfrac{\overline{\eta}_d}{\overline{\eta}_a} - \dfrac{\overline{\eta}_a}{\overline{\eta}_d} \right) - \left(\dfrac{\overline{\eta}_a}{\overline{\eta}_d} + \dfrac{\overline{\eta}_d}{\overline{\eta}_a} \right) p \right]}{1 + \dfrac{1}{2\sqrt{1-p^2}} \left[\left(\dfrac{\overline{\eta}_d}{\overline{\eta}_a} + \dfrac{\overline{\eta}_a}{\overline{\eta}_d} \right) + \left(\dfrac{\overline{\eta}_a}{\overline{\eta}_d} - \dfrac{\overline{\eta}_d}{\overline{\eta}_a} \right) p \right]} \tag{21}$$

where we have defined the function

$$p \equiv \frac{Y}{2\Psi} = \frac{B/2}{\sin(k_0 c n_d \cos\theta_d) + \cos(k_0 c n_d \cos\theta_d)(B/2)}. \tag{22}$$

We will concentrate on analyzing Γ_∞ in the rest of this paper.

In Fig. 3(a) we plot the bulk reflectivity off the semi-infinite PBG medium. We also plot the quantity $|\tau|$ (12), providing the bandgaps that are marked by the heavy line in the figure. We observe that in the bandgaps the reflectivity is close to 100%. In Fig. 3(b), we plot the real and imaginary parts of the bulk reflection coefficient. Notice that, *unlike in normal conducting or dielectric media*, Γ_∞^r is positive within half of each bandgap as well as outside the corresponding band edge. At these frequencies, the medium looks like a magnetic conductor approaching a perfect magnetic wall at the corresponding band edges. This is very important since it implies that the incident and reflected fields add in phase and the total tangential electric field near

$$k_0 c \leq \frac{\sqrt{\sin^2\theta + ((n_d^r)^2 - \sin^2\theta) \left[\left(\dfrac{m\pi c}{a} \right)^2 - 1 \right] + \left(\dfrac{2n\pi c}{a} \right)^2 (n_d^r)^2} + \dfrac{2n\pi c}{a} \sin\theta}{(n_d^r)^2 - \sin^2\theta} \tag{18}$$

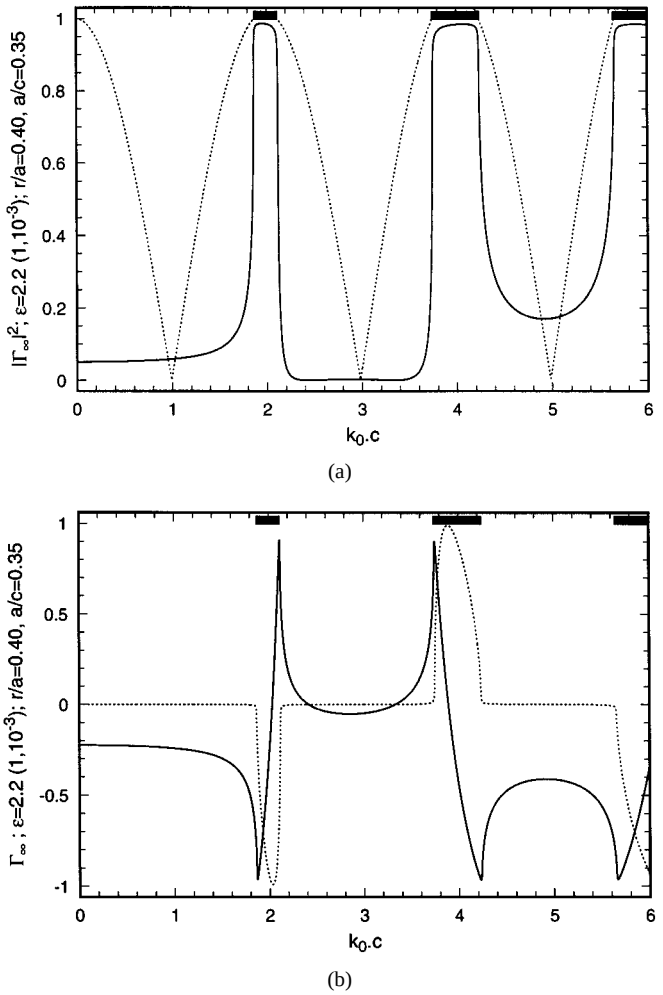

Fig. 3. (a) Reflectivity of the semi-infinite PBG medium (solid) and $|\tau|$ (dotted). The bandgaps are the regions marked with the thick solid line and (b) real (solid) and imaginary (dotted) parts of the semi-infinite reflection coefficient.

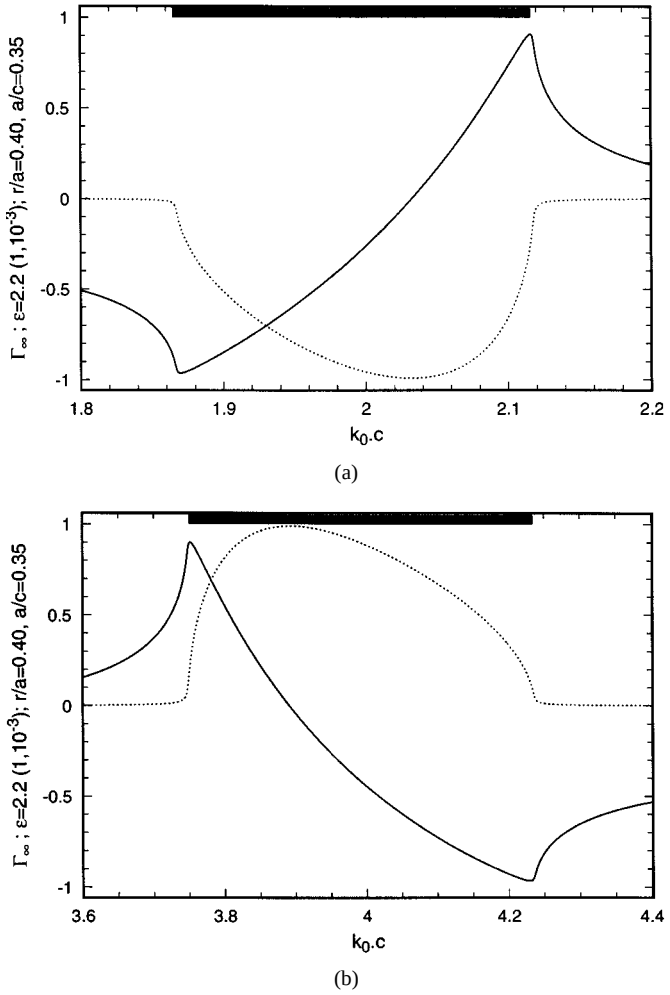

Fig. 4. Real (solid) and imaginary (dotted) parts of the semi-infinite reflection coefficient in: (a) the first bandgap and (b) the second bandgap.

the PBG medium surface is not reduced (or close to zero), as in normal media.

In Fig. 4 we expand the plots to show detail in the first and second bandgaps. Comparing the situation to that of a good conductor, we observe that the PBG medium creates a strong dispersive variation on the total tangential field, ranging from the behavior of an electric wall (very good conductor, $\Gamma^r_\infty \simeq -1$ nodes on $\boldsymbol{E}_t$) to that of a magnetic wall, where $\Gamma^r_\infty \simeq +1$ and $\boldsymbol{E}_t$ become maximum. This phenomenon should be of considerable practical importance in applications relating to phase-advance media. The bandgaps for the parameter values chosen, are of constant bandwidth of about 12%.

III. Effective Wave Impedance of Printed PBG Media

In this section, we provide the fundamentals for deriving the effective response functions, confining ourselves to the semi-infinite case for normal incidence, which will provide a corresponding effective wave impedance. We therefore drop the bars from the η's for normal incidence in the rest of this paper.

A. Effective Wave Impedance from Bulk Reflection

By inspection, (21) can be rewritten as

$$\Gamma_\infty = \frac{\dfrac{\eta_d}{\eta_a}\dfrac{(1-p)}{\sqrt{1-p^2}} - \dfrac{\eta_a}{\eta_d}\dfrac{(1+p)}{\sqrt{1-p^2}}}{2+\dfrac{\eta_d}{\eta_a}\dfrac{(1-p)}{\sqrt{1-p^2}} + \dfrac{\eta_a}{\eta_d}\dfrac{(1+p)}{\sqrt{1-p^2}}} = \frac{\left(\dfrac{\eta_d}{\eta_a}\dfrac{(1-p)}{\sqrt{1-p^2}}\right)^2 - 1}{\left(\dfrac{\eta_d}{\eta_a}\dfrac{(1-p)}{\sqrt{1-p^2}}+1\right)^2} = \frac{\eta_d\dfrac{(1-p)}{\sqrt{1-p^2}} - \eta_a}{\eta_d\dfrac{(1-p)}{\sqrt{1-p^2}} + \eta_a}. \quad (23)$$

This formula is identical to the formula giving the bulk reflection coefficient for a macroscopically homogeneous medium of relative effective wave impedance

$$\eta_{\text{eff}} = \eta_d\frac{(1-p)}{\sqrt{1-p^2}} \quad (24)$$

where p is given in (22).

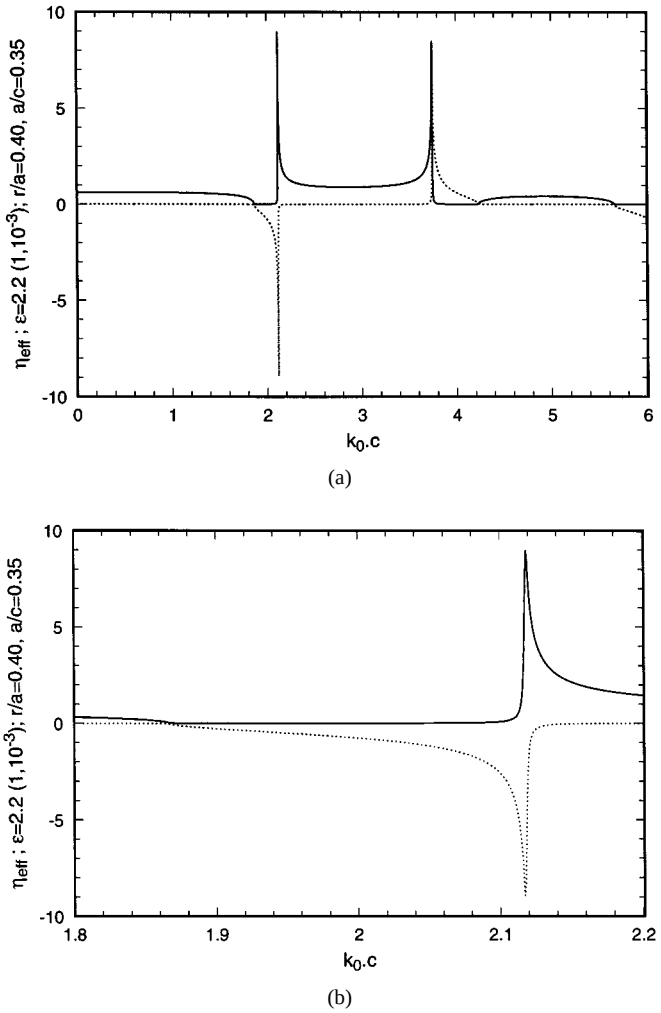

Fig. 5. (a) Real (solid) and imaginary (dotted) parts of relative effective wave impedance of PBG medium and (b) same as in (a) in the first bandgap.

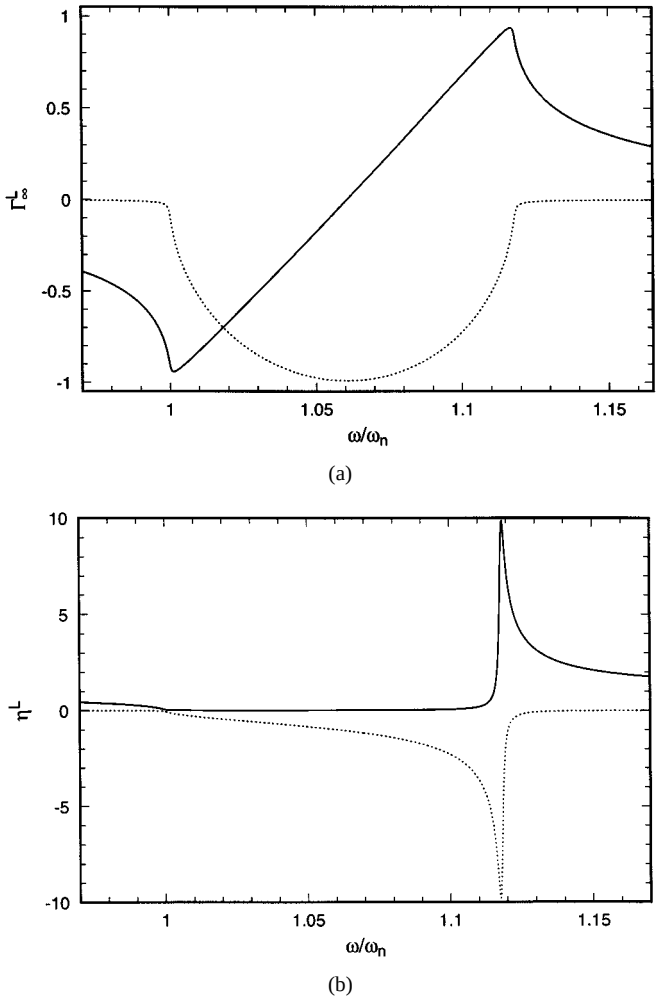

Fig. 6. (a) Real (solid) and imaginary (dotted) parts of the bulk reflection coefficient generated by a point-like Lorentzian permittivity and (b) same as in (a) for the wave impedance.

In Fig. 5, we plot the function η_{eff} for normal plane-wave incidence. We observe that the impedance is completely resistive outside the bandgaps and has strong resonant behavior inside the bandgaps, becoming completely capacitive or inductive. At the band edges, very strong resonances (of the order of 4 KΩhms) are produced.

B. Artificial versus Natural Crystals: Lorentzian Description

In advancing the effective description of PBG materials further, we wish to explore the natural similarities these materials *should* have, with natural crystals. It has been shown that the latter are very well described by permittivity tensors that are driven by the oscillations of electrons bound to the lattice ions [23]. Effectively, a quantum electrodynamics description of the interactions between these bound electrons and the electromagnetic field yields the classical Lorentz oscillator model, which gives rise to these permittivity tensors [24], with the important advantage being that it predicts the Lorentzian parameters in terms of a few fundamental physical constants.

If our analogy with natural crystals is tenable beyond the obvious similarity used up to now in the literature relating to the periodic geometry, the behavior of the bulk reflection coefficient and wave impedance for the PBG medium, shown in Figs. 4(a) and 5(b), should resemble that of a point-like Lorentzian permittivity. To establish that, in Fig. 6 we show the corresponding plots produced by a Lorentzian permittivity ϵ^L, arbitrarily normalized in frequency (ω_n) of the form

$$\epsilon^L = 1 + \mathcal{L}(\omega)$$
$$\mathcal{L}(\omega) = \frac{(\omega_p/\omega_n)^2}{(\omega_0/\omega_n)^2 - (\omega/\omega_n)^2 + j(\omega/\omega_n)(\gamma/\omega_n)}. \quad (25)$$

Choosing the normalized width $\gamma/\omega_n = 0.001$, similar to the loss tangent of the PBG medium host dielectric, the resonance $\omega_0/\omega_n = 1$, and the plasma frequancy $\omega_p/\omega_n = 0.5$, we observe that the respose of the PBG medium at and around a bandgap is *very similar* to that of a single point-like Lorentzian crystal.

Multiple bandgaps in the artificial crystal correspond to multiple Lorentzians in the natural crystal. The latter are generated by absorption of the incident photon by the bound electron, which is excited from an initial state $|a>$ to a number of different intermediate states $\{|i>\}$. Subsequently, the excited electron returns to a final state $|b>$ by emmiting a photon. These excitations are distinguished by the spectrum of intermediate

states $\{|i>\}$ (determined by the nature of the crystal), which fixes the allowed resonant energies (frequencies) of the incident photon (field). In short, each bandgap of the artificial crystal corresponds to one Lorentzian excitation in the natural crystal.

There are, of course, some differences between the artificial PBG medium and a natural crystal: In the former, the induced currents and multipole moments are distributed on the whole surface (or volume, for dielectric implants) of the scatterers, while in the latter the multipole moments are point-like: they arise from the "induced current" due to the motion of the point-like electron charge under the influence of the incident photon field. The multipole expansion of the scattered field off the artificial implants corresponds in the natural crystal to expectation values of tensor products of the electron momentum $(\boldsymbol{p})$ and position $(\boldsymbol{r})$ operators between the electron initial and final states. To be specific, there is the precise correspondence (taking as an example spontaneous emission)

electric dipole transitions

$$\frac{2e}{m}\langle b|\boldsymbol{p}|a\rangle \leftrightarrow \int \boldsymbol{J}(\boldsymbol{r})\, d^3r \tag{26}$$

electric quadrupole transitions

$$\frac{2e}{m}\langle b|\boldsymbol{rp}+\boldsymbol{pr}|a\rangle \leftrightarrow \int [\boldsymbol{rJ}(\boldsymbol{r})+\boldsymbol{J}(\boldsymbol{r})\boldsymbol{r}]\, d^3r \tag{27}$$

magnetic dipole transitions

$$\frac{2e}{m}\langle b|\boldsymbol{r}\times\boldsymbol{p}+\frac{h}{8\pi v}\,\sigma|a\rangle \leftrightarrow \int \boldsymbol{r}\times\boldsymbol{J}(\boldsymbol{r})\, d^3r \tag{28}$$

where $\boldsymbol{J}$ is the volume current density integrated over the scatterer volume, while $\boldsymbol{\sigma} = \{\sigma_1, \sigma_2, \sigma_3\}$ are the Pauli spin matrices given in the Appendix and e, m, h, v the electron charge, mass, Planck's constant, and speed of light, respectively. Notice, in particular, that the magnetic dipole term in (28) is generated by two terms—the first relating to the angular momentum operator (which directly corresponds to the surface current density in the artificial crystal) and the second relating to the electron spin, which has no analogue in terms of current densities. In the artificial crystal case, the multipole terms above have to be integrated over the scatterer volume, while in the natural crystal case these terms arise from operators evaluated between the electron states. This and related differences result in the "distributed" nature of the PBG medium versus the point-like behavior of the natural crystal, as shown in the comparison between Figs. 4(a) and 6(a).

It is essential to notice that *there is* a Lorentzian that generates the functions Γ_∞ and η_{eff} (23), (24); this is the function p [see (22)], which is plotted in Fig. 7. We notice, in particular, in the detailed plot of Fig. 7(b) (within the first bandgap) that the shape and relative normalization of p^r, p^i is *exactly* that of a Lorentzian permittivity function. It is of interest to observe that in the natural crystal, the Lorentzian permittivity results from the forward scattering amplitude through the use of the optical theorem. The scattering amplitude itself, to leading order in perturbation theory, results from the Kramers–Heisenberg quantum-mechanical formula [24]. That formula allows for an one-to-one correspondence between the quantum-mechanical Lorentzian and our generating function p for the PBG medium.

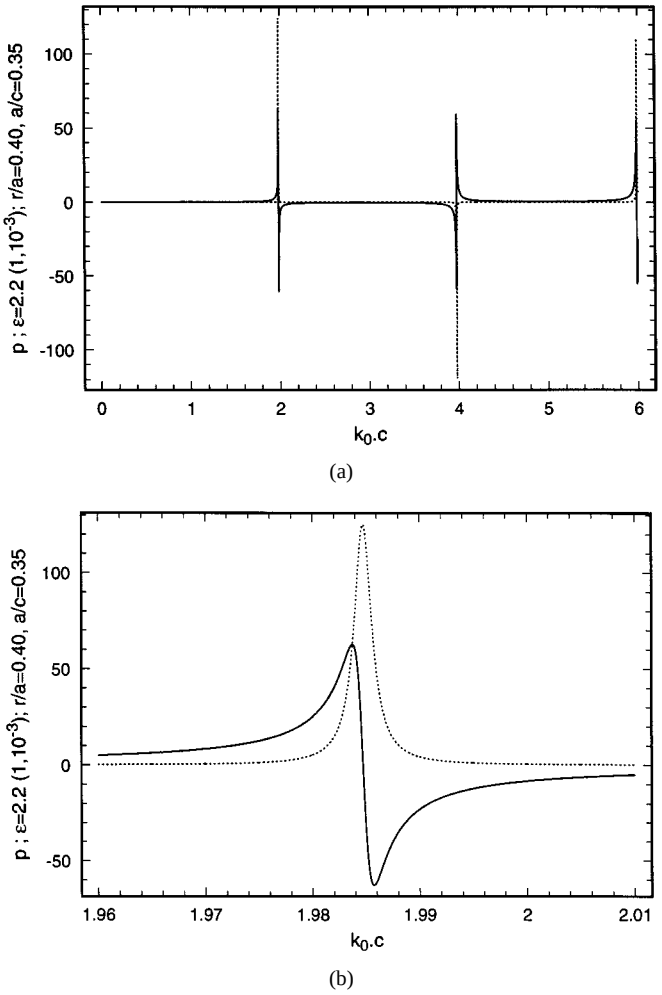

Fig. 7. (a) Real (solid) and imaginary (dotted) parts of the generating function p and (b) same as in (a) in the first bandgap.

In the following, we will fit this function with a correctly scaled sum of Lorentzians. The Lorentzian behavior in the function p is produced by the resonant denominator Ψ (22). For normal incidence, the frequency scale is introduced through the variable

$$\begin{aligned} k_0 c n_d &\equiv x_1 - j x_2, \\ x_1 &\equiv k_0 c n_d^r \\ x_2 &\equiv k_0 c n_d^r \tan\delta/2 \end{aligned} \tag{29}$$

where $\tan\delta$ is the loss tangent of the dielectric host. To accurately calculate the resonant frequencies, we can set $x_2 = 0$. Defining the positive constant

$$A = \frac{B}{2k_0 c n_d} \tag{30}$$

with B given by the first equality in (15), we obtain

$$p \simeq \frac{A x_1}{\sin x_1 + A x_1 \cos x_1}. \tag{31}$$

Because A is small, the poles of this function are located near $x_1 \simeq m\pi$, where m is an integer. To determine the resonant frequencies, we write $x_1^{(m)} \simeq m\pi - \epsilon_m$, expand the denominator

of (31) to leading order in ϵ_m, and set the real part to zero. This gives us

$$\epsilon_m \simeq \frac{m\pi A}{1+A}, \qquad x_1^{(m)} \simeq \frac{m\pi}{1+A}. \tag{32}$$

We will write the Lorentzian fit covering the first three bandgaps as

$$p \simeq p_L \equiv p_0 + \sum_{m=1}^{3} (-1)^{m-1} \mathcal{L}_m \tag{33}$$

where we have (34), shown at the bottom of the page.

In this equation, fine-tuning beyond the second decimal is achieved through the small parameters ϵ_p, ϵ_0, ϵ_γ, which correspond to precision-adjustment of the effective plasma frequency, resonant frequency, and width. The constant p_0 in (33) is obtained from the sum rule

$$\lim_{k_0 c \to 0} p_L = \lim_{k_0 c \to 0} p = \frac{A}{1+A} \tag{35}$$

and it fine-tunes the plateaus of p outside the bandgaps. For our usual choice of lattice and scatterer size, we find

$$\begin{aligned} &\epsilon_p^{(1)} = 0.08, \quad \epsilon_p^{(2)} = 0.04, \quad \epsilon_p^{(3)} = -0.0266 \\ &\epsilon_0^{(1)} = 0.001\,67, \quad \epsilon_0^{(2)} = 0.006\,28, \quad \epsilon_0^{(3)} = 0.012\,94 \\ &\epsilon_\gamma^{(1)} = 0.025, \quad \epsilon_\gamma^{(2)} = 0.015, \quad \epsilon_\gamma^{(3)} = 0.015. \end{aligned} \tag{36}$$

We can now bring (34) in the form of (25), writing

$$\mathcal{L}_m(\omega) = \frac{(\omega_p^{(m)}/\omega_n)^2}{(\omega_0^{(m)}/\omega_n)^2 - (\omega/\omega_n)^2 + j(\omega/\omega_n)(\gamma^{(m)}/\omega_n)} \tag{37}$$

where

$$\begin{aligned} \frac{\omega}{\omega_n} &= k_0 c, \\ \frac{\omega_p^{(m)}}{\omega_n} &= \frac{m}{n_d^r}\sqrt{1+\epsilon_p^{(m)}} \\ \frac{\omega_0^{(m)}}{\omega_n} &= \frac{m\pi}{(1+A)n_d^r}\sqrt{1+\epsilon_0^{(m)}} \\ \frac{\gamma^{(m)}}{\omega_n} &= m\frac{\tan\delta}{2n_d^r}\left(1+\left(\frac{\pi A}{1+A}\right)^{-1}\right)(1+\epsilon_\gamma^{(m)}) \end{aligned} \tag{38}$$

while p_0 in (33) is given by

$$p_0 = \frac{A}{1+A} + \sum_{m=1}^{3} (-1)^m \left(\frac{\omega_p^{(m)}}{\omega_0^{(m)}}\right)^2. \tag{39}$$

In Fig. 8(a)–(c) we compare the functions p and p_L in the bandgaps. The agreement is perfect and the difference between p and p_L cannot be distinguished in the plots.

It is important to notice that the various terms in the sum of (33) are roughly the same Lorentzian function, scaled in frequency by an integer multiple of the fundamental frequency of the first bandgap, as indicated by the formula providing the resonant frequencies, (32). An alternative parametrization, which introduces the scaling of the shape in the Lorentzian width rather than the plasma frequency, gives equally perfect agreement. In this latter case

$$\frac{\omega_p^{(m)}}{\omega_0^{(m)}} \simeq \frac{1}{m}\frac{(1+A)}{\pi}. \tag{40}$$

The difference between these alternatives is formal only, since it would affect the sum rule (33) if the summation were to be extended to infinity. For the purposes of this paper, that alternative would not be more useful than our current fit since we are only concerned with the range of validity of our theory, which is bounded by (19). For formal considerations of causality, however, this second alternative would be preferable since the Kramers–Kronig relations would need the behavior of the effective response functions at $\omega \to \infty$ and one would have to extend the summation of the Lorentzians to infinity, even for proving causality within our finite range of validity. In this case, the summation in (39) would be strongly convergent if (39) were used instead

$$\begin{aligned} \sum_{m=1}^{\infty} (-1)^m \left(\frac{\omega_p^{(m)}}{\omega_0^{(m)}}\right)^2 &= \frac{(1+A)^2}{\pi^2}\sum_{m=1}^{\infty}\frac{(-1)^m}{m^2} \\ &= -\frac{(1+A)^2}{2\pi^2}\zeta(2) \\ &= -\frac{(1+A)^2}{12} \end{aligned} \tag{41}$$

where the Riemann zeta function $\zeta(2) = \pi^2/6$ has been used. We will not explore the consequences of Lorentzian fit uniqueness to causality any further in this paper.

We will now show that each bandgap is driven *primarily* by the corresponding Lorentzian in the sum of (33), despite the complicated dependence of Γ_∞ and η_{eff} on the *sum* of $\mathcal{L}_m$, i.e., $\mathcal{L}_m$ act like distributions. The above remark, coupled with the agreement between the actual response of the PBG medium [Fig. 4(a)] and the single Lorentzian medium [Fig. 6(a)], allows us to find a very simple formula giving the approximate position and size of a specific bandgap as driven by the corresponding single Lorentzian (37).

$$\mathcal{L}_m = \frac{m^2(1+\epsilon_p^{(m)})}{\left(\frac{m\pi}{1+A}\right)^2(1+\epsilon_0^{(m)}) - x_1^2 + jx_2 m\left(1+\frac{\pi A}{1+A}\right)\left(\frac{\pi A}{1+A}\right)^{-1}(1+\epsilon_\gamma^{(m)})} \tag{34}$$

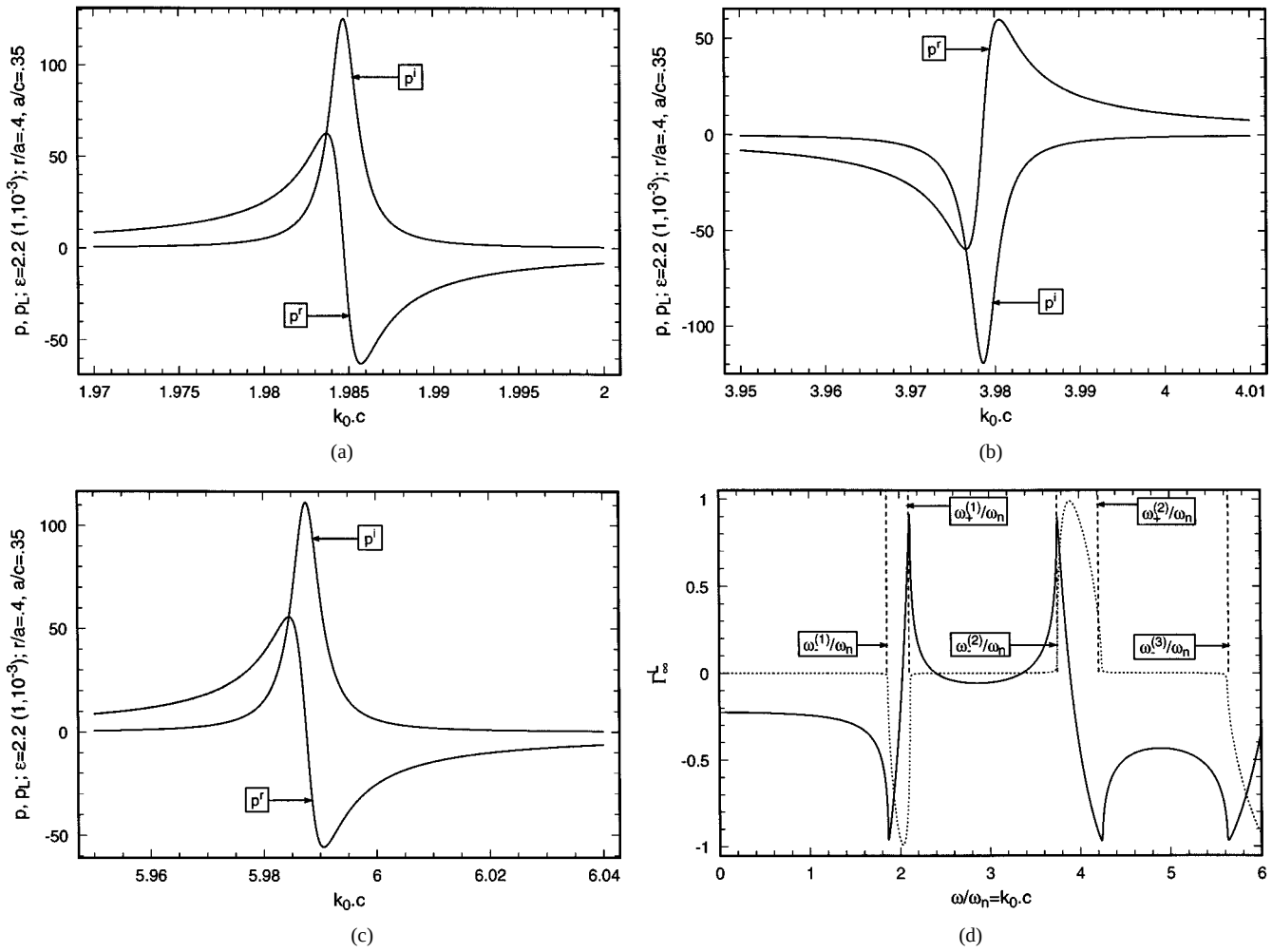

Fig. 8. Comparison between the exact function p (solid) and its Lorentzian approximation p_L (dotted) in the (a) first, (b) second, and (c) third bandgap. (d) Real (solid) and imaginary (dotted) parts of the effective bulk reflection coefficient generated from the Lorentzian function p_L and Lorentzian calculation of the band edges (dashed lines).

For the Lorentzian of (25), the band edges are given at frequencies

$$\frac{\omega_\pm}{\omega_n}: \mathrm{Re}\{\epsilon^L(\omega_\pm)\} = 1 + \mathrm{Re}\{\mathcal{L}(\omega_\pm)\} = 0. \tag{42}$$

In our case, the effective impedance (24) yields an equivalent Lorentzian permittivity

$$\frac{1}{(\eta_{\text{eff}}/\eta_d)^2} = \frac{1+p_L}{1-p_L}. \tag{43}$$

Therefore, the band edges of the mth bandgap are *approximately* determined by the Lorentzian function (44), shown at the bottom of the page. From (42) and (44) we derive the band edges of the system

$$\begin{aligned}\left(\frac{\omega_\pm^{(m)}}{\omega_n}\right)^2 &= \left[\left(\frac{\omega_0^{(m)}}{\omega_n}\right)^2 + (-1)^m\left(\frac{\omega_p^{(m)}}{\omega_n}\right)^2\right] \\ &\quad - \frac{1}{2}\left[2(-1)^m\left(\frac{\omega_p^{(m)}}{\omega_n}\right)^2 + \left(\frac{\gamma^{(m)}}{\omega_n}\right)^2\right] \\ &\quad \pm \left\{\left(\frac{1}{2}\left[2(-1)^m\left(\frac{\omega_p^{(m)}}{\omega_n}\right)^2 + \left(\frac{\gamma^{(m)}}{\omega_n}\right)^2\right]\right)^2 \right. \\ &\quad - \left(\frac{\gamma^{(m)}}{\omega_n}\right)^2\left[\left(\frac{\omega_0^{(m)}}{\omega_n}\right)^2 \right. \\ &\quad \left.\left. + (-1)^m\left(\frac{\omega_p^{(m)}}{\omega_n}\right)^2\right]\right\}^{1/2}\end{aligned} \tag{45}$$

$$\frac{1+(-1)^{m-1}\mathcal{L}_m}{1-(-1)^{m-1}\mathcal{L}_m} = 1 + \frac{(-1)^{m-1}2(\omega_p^{(m)}/\omega_n)^2}{[(\omega_0^{(m)}/\omega_n)^2 - (-1)^{m-1}(\omega_p^{(m)}/\omega_n)^2] - (\omega/\omega_n)^2 + j(\omega/\omega_n)(\gamma^{(m)}/\omega_n)} \tag{44}$$

and bandgap size $\Gamma_{\rm PBG}^{(m)}$

$$\frac{\Gamma_{\rm PBG}^{(m)}}{\omega_n} = \frac{\omega_+^{(m)}}{\omega_n} - \frac{\omega_-^{(m)}}{\omega_n} \tag{46}$$

where ω_n is given by the first equality in (38).

In Fig. 8(d), we plot the real and imaginary parts of the effective bulk reflection coefficient generated by the function p_L and the band edges provided by the Lorentzian approximation (45). The agreement with the exact results of Fig. 3(a) is, again, excellent. It should be pointed out that an algebraic solution for the band edges through the exact equation $|\tau| = 1, \tau$, given by (14), is impossible since this is a transendental equation. Instead, through the use of Lorentzians, one trivially arrives at the algebraic solution of (45).

IV. Conclusions

We have approached composite electromagnetic media via an analytical method based on multipole expansions and transfer-matrix theory for the observables of the system. We have also shown that an effective description of these media is possible, far beyond the confines of EMT, at the order of a unit-cell size equal to the free-space wavelength. We have demonstrated the effectiveness of our approach by deriving the effective wave impedance of a practical PBG medium, an orthogonal lattice of thin PEC disks embedded in a lossy host dielectric.

We have found that the bulk reflection coefficient is dramatically dispersive as we cross the bandgaps of the medium ranging approximately in values from $(-1, 0)$ to $(+1, 0)$. The system exhibits frequency-dependent electromagnetic transitions from an electric wall to a magnetic wall, with corresponding nodes or antinodes on the total electric field near the surface. The effective wave impedance is similarly very dispersive, with a resistive part ranging from zero (inside the bandgaps) to 4000 Ω hms (at the band edges) and a complementary reactive part, which is alternatively capacitive or inductive within successive bandgaps.

Finally, we have established a correspondence with natural crystals, beyond mere geometrical analogies. Namely, we have shown that printed photonic crystals are effectively described by Lorentzian functions that generate the wave impedance and bulk reflectivity in the same way that natural crystals are described by Lorentzian functions resulting from the interactions of photons with bound electrons in quantum electrodynamics. We have provided a Lorentzian response function that accurately reproduces the effective impedance and bulk reflection coefficient. This Lorentzian approach also provides accurately the band edges of the system in a simple closed algebraic form and readily lends itself to a circuit interpretation for PBG media since Lorentzians are oscillatory excitations made up of lumped circuit elements.

Appendix
Calculation of U^N

Define a triplet of 2×2 complex traceless matrices $\{\sigma_i\} = \{\sigma_1, \sigma_2, \sigma_3\}$, known as the Pauli spin matrices [25]

$$\sigma_1 = \begin{pmatrix} 0 & 1 \\ 1 & 0 \end{pmatrix}$$
$$\sigma_2 = \begin{pmatrix} 0 & j \\ -j & 0 \end{pmatrix}$$
$$\sigma_3 = \begin{pmatrix} 1 & 0 \\ 0 & -1 \end{pmatrix}. \tag{47}$$

The σ's are the generators of the rotation group of two-component complex fields in three spatial dimensions [26] known as SU(2). In our formulation, the layers transform the field amplitudes $\{R, L\}$ and these transformations constitute a group containing SU(2).

Let us employ the summation convention that repeated indices are summed over their range (e.g., $A_{ik}B_{lmk} \equiv \Sigma_{k=1}^{3} A_{ik}B_{lmk}$). An important property of the σ's is the algebra

$$\sigma_i\sigma_j = -j\epsilon_{ijk}\sigma_k + \delta_{ij}\mathbf{1} \tag{48}$$

where ϵ_{ijk} is the fully antisymmetric Levi–Civita tensor, specified in terms of even and odd permutations (P_e or P_o) of its indexes

$$\epsilon_{ijk} = \begin{cases} +1, & \text{if } (ijk) = P_e(123); \\ -1, & \text{if } (ijk) = P_o(123); \\ 0, & \text{otherwise} \end{cases} \tag{49}$$

and δ_{ij} is the Kronecker delta. We can expand the matrix U in terms of the set of matrices $\{\mathbf{1}, \sigma_i\}$

$$U = z_0\mathbf{1} + z_i\sigma_i = z_0(\mathbf{1} + \zeta_i\sigma_i), \qquad \zeta_i \equiv \frac{z_i}{z_0} \tag{50}$$

where, by inspection

$$z_0 = \tfrac{1}{2}(U_{11} + U_{22}), \qquad z_1 = \tfrac{1}{2}(U_{12} + U_{21})$$
$$z_2 = -\frac{j}{2}(U_{12} - U_{21}), \qquad z_3 = \frac{1}{2}(U_{11} - U_{22}). \tag{51}$$

Raising U to the Nth power will involve even or odd multilinears of $\zeta_i\sigma_i$, which we write symbolically as $(\zeta_i\sigma_i)^{2k}, (\zeta_i\sigma_i)^{2k+1}$. Notice that

$$(\zeta_i\sigma_i)^{2k} = (\zeta_i\sigma_i\zeta_j\sigma_j)^k. \tag{52}$$

Using the algebra (48) and the fact that the contraction of a product of a symmetric and an antisymmetric tensor on a pair of indexes is zero, we get (from now on, we will suppress the matrix $\mathbf{1}$ from all equations)

$$\begin{aligned}\zeta_i\sigma_i\zeta_j\sigma_j &= \zeta_i\zeta_j\sigma_i\sigma_j = \zeta_i\zeta_j[-j\epsilon_{ijk}\sigma_k + \delta_{ij}] \\ &= -j\zeta_i\zeta_j\epsilon_{ijk}\sigma_k(=0) + \zeta_i\zeta_i \equiv \hat{\zeta}^2\end{aligned} \tag{53}$$

which leads to

$$(\zeta_i\sigma_i)^{2k} = (\hat{\zeta}^2)^k, \quad (\zeta_i\sigma_i)^{2k+1} = \zeta_i\sigma_i(\hat{\zeta}^2)^k. \tag{54}$$

Hence, U^N can be expanded through the binomial expansion as if $\zeta_i\sigma_i$ were a number

$$\begin{aligned}U^N &= z_o^N[P_0(\hat{\zeta}^2) + \zeta_i\sigma_i P_1(\hat{\zeta}^2)] \\ &= z_0^N\left[P_0(\hat{\zeta}^2) - P_1(\hat{\zeta}^2) + U\frac{P_1(\hat{\zeta}^2)}{z_0}\right]\end{aligned} \tag{55}$$

where the polynomials P_0, P_1 are the even and odd binomial projections

$$(1+x)^N = P_0(x^2) + xP_1(x^2) \rightarrow$$
$$P_0(x^2) = \sum_{k=0}^{[N/2]} \frac{N!}{(2k)!(N-2k)!}(x^2)^k;$$
$$P_1(x^2) = \sum_{k=0}^{[(N-1)/2]} \frac{N!}{(2k+1)!(N-2k-1)!}(x^2)^k. \quad (56)$$

We may now sum up the polynomials $P_1(\hat{\zeta}^2), P_0(\hat{\zeta}^2)$. Denote the "positive" square root (by "positive" we mean the one whose real part is positive) of $\hat{\zeta}^2$ by $\zeta = \sqrt{\hat{\zeta}^2}$. Then

$$(1 \pm \zeta)^N = P_0(\hat{\zeta}^2) \pm \zeta P_1(\hat{\zeta}^2) \quad (57)$$

and, hence

$$P_0(\hat{\zeta}^2) = \tfrac{1}{2}[(1+\zeta)^N + (1-\zeta)^N]$$
$$P_1(\hat{\zeta}^2) = \frac{1}{2\zeta}[(1+\zeta)^N - (1-\zeta)^N]. \quad (58)$$

REFERENCES

[1] C. M. Soukoulis, Ed., *Photonic Band Gaps and Localization*. ser. NATO ASI Ser. B. New York: Plenum, 1993, vol. 308.

[2] "Development and applications of materials exhibiting photonic band gaps," *J. Opt. Soc. Amer. B—Special Issue*, vol. 10, 1993.

[3] C. M. Soukoulis, Ed., *Photonic Band Gap Materials—Applied Sciences*. ser. NATO ASI Ser. E. Boston, MA: Kluwer, 1996, vol. 315.

[4] N. G. Alexopoulos and D. R. Jackson, "Fundamental superstrate effects on printed circuit antennas," *IEEE Trans. Antennas Propagat.*, vol. AP-32, pp. 807–816, Aug. 1984.

[5] N. G. Alexopoulos, D. R. Jackson, and P. B. Katehi, "Criteria for nearly omnidirectional radiation patterns for printed antennas," *IEEE Trans. Antennas Propagat.*, vol. AP-33, pp. 195–205, Feb. 1985.

[6] H. Y. Yang and N. G. Alexopoulos, "Gain enhancement methods for printed circuit antennas through multiple superstrates," *IEEE Trans. Antennas Propagat.*, vol. AP-35, pp. 860–863, July 1987.

[7] H. Y. Yang, N. G. Alexopoulos, and E. Yablonovitch, "Photonic band-gap materials for high-gain printed circuit antennas," *IEEE Trans. Antennas Propagat.*, vol. 45, pp. 185–187, Jan. 1997.

[8] H. Contopanagos, N. G. Alexopoulos, and E. Yablonovitch, "High Q radio frequency structures using one-dimensionally periodic metallic films," *IEEE Trans. Microwave Theory Tech.*, vol. 46, pp. 1310–1312, Sept. 1998.

[9] H. Y. Yang, N. G. Alexopoulos, and R. E. Diaz, "Reflection and transmission of waves from multilayer structures with planar-implanted periodic material blocks," *J. Opt. Soc. Amer. B*, vol. 14, no. 10, pp. 2513–2519, Oct. 1997.

[10] S. Fan, P. R. Villeneuve, and J. D. Joannopoulos, "XQXQXQ," *Phys. Rev.*, vol. B54, p. 11 245, 1996.

[11] J. B. Pendry, "Calculating photonic band gap structures," *J. Phys. Condens. Matter 8*, p. 1086, 1996.

[12] D. R. Smith, S. Schultz, N. Kroll, M. Sigalas, K. M. Ho, and C. M. Soukoulis, "Experimental and theoretical results for a two-dimensional metal photonic band gap cavity," *Appl. Phys. Lett.*, vol. 65, p. 645, 1994.

[13] R. Coccioli, T. Itoh, and G. Pelosi, "A finite element-generalized network analysis of finite thickness photonic crystals," *1997 IEEE MTT—S Dig.*, pp. 195–198.

[14] E. W. Lucas and T. P. Fontana, "A 3-D hybrid finite element/boundary element method for the unified radiation and scattering analysis of general infinite periodic arrays," *IEEE Trans. Antennas Propagat.*, vol. 43, pp. 145–153, Feb. 1995.

[15] S. D. Gedney, J. F. Lee, and R. Mittra, "A combined FEM/MoM approach to analyze the plane wave diffraction by arbitrary gratings," *IEEE Trans. Antennas Propagat.*, vol. 40, pp. 363–370, Feb. 1992.

[16] H. Contopanagos, L. Zhang, and N. G. Alexopoulos, "Thin frequency selective lattices integrated in novel compact MIC, MMIC and PCA architectures," *IEEE Trans. Microwave Theory Tech.*, vol. 46, pp. 1936–1948, Sept. 1998.

[17] Y. Qiu and K. M. Leung, "Complex band structure and transmission spectra of two dimensional photonic crystals," *SPIE*, vol. 2117, p. 32, 1994.

[18] K. Sakoda, "Optical transmittance of a two-dimensional triangular photonic lattice," *Phys. Rev.*, vol. B51, p. 4672, 1995.

[19] K. Sakoda, "Transmittance and Bragg reflectivity of two-dimensional photonic lattices," *Phys. Rev.*, vol. B52, p. 8992, 1995.

[20] R. E. Collin, *Field Theory of Guided Waves*, 2nd ed. New York: IEEE Press, 1991, pp. 771–772.

[21] M. Born and E. Wolf, *Principles of Optics*, 4th ed. Oxford, UK: Pergamon, 1970, pp. 66–70.

[22] G. Matthaei, L. Young, and E. M. T. Jones, *Microwave Filters, Impedance-Matching Networks and Coupling Structures*. Norwood, MA: Artech House, 1980, p. 238.

[23] C. Bohren and D. Huffman, *Absorption and Scattering of Light by Small Particles*. New York: Wiley, 1983, pp. 227–251.

[24] J. J. Sakurai, *Advanced Quantum Mechanics*. Menlo Park, CA: Benjamin/Cummings, 1984, pp. 41–64.

[25] W. Pauli, "Zur quantenmechanik des magnetischen elektrons," *Z. Physik*, vol. 43, p. 601, 1927.

[26] E. Wigner, *Group Theory and its Application to the Quantum Mechanics of Atomic Spectra*. New York: Academic, 1959, pp. 157–170.

Chryssoula A. Kyriazidou (M'98) received the B.S. degree in physics from the University of Athens, Greece, in 1984, and the M.S. and Ph.D. degrees in physics from the University of Michigan, Ann Arbor, in 1989 and 1992, respectively. She is currently working toward the Ph.D. degree in electrical engineering at the University of California, Los Angeles.

She worked as a Postdoctoral Research Associate with the High Energy Physics Group at Brookhaven National Laboratory from 1992 to 1993 and at Argonne National Laboratory from 1993 to 1996. Her research then included quantum field theory with an emphasis on quantum radiative corrections to electroweak scattering processes. She has authored 15 publications in the area of electromagnetics. Her current research interests include novel composite materials, photonic bandgap structures, novel antenna design and monolithics microwave integrated circuits (MMIC's), accelerated full-wave codes for electromagnetic simulations, and signal propagation in urban media.

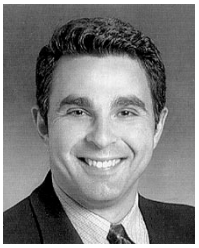

Harry F. Contopanagos (M'98) received the B.S. degree in physics from the National University of Athens, Greece, in 1984, and the M.S. and Ph.D. degrees in physics from the University of Michigan at Ann Arbor, in 1989 and 1991, respectively.

From 1991 to 1993, he worked as a Research Associate at the Institute for Theoretical Physics, SUNY Stony Brook, Long Island, NY, where he performed research on scattering theory in quantum electrodynamics and quantum chromodynamics. From 1993 to 1996, he was a Research Associate in Argonne National Laboratory where he provided theoretical predictions for the production cross section of the newly discovered top quart, in excellent agreement with subsequent experiments. He worked as a Research Engineer with the Electrical Engineering Department, University of California Los Angeles, from 1996 to 1999. He is currently a Senior Research Scientist at Hughes Research Laboratories, Malibu, CA. His recent research activities include theory and fabrication of composite electromagnetic media, applications in compact high-frequency waveguide filters, printed antennas, physical modeling of communication channels, integral equations and fast numerical implementations. He has authored 15 publications in the area of electromagnetics and 30 publications in the area of high-energy physics.

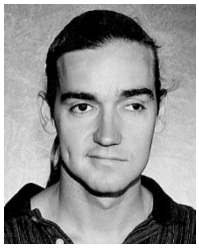

William M. Merrill (S'96) was born in Scottsdale, AZ, in 1972. He received the B.S. degree (honors) in electrical and computer engineering from the University of Arizona, Tempe, in 1994, and the M.S.E.E. degree from the University of California at Los Angeles (UCLA), in 1996. He is currently working toward the Ph.D. degree in electrical engineering at UCLA.

Since 1994 he has been employed as a Graduate Student Researcher at UCLA. He is the author or coauthor of 16 journal and conference publications. His current research interests include propagation through complex systems, ordered and disordered complex media, percolation theory, artificial crystals exhibiting photonic bandgaps, and the electromagnetic response of self-similar (fractal) structures.

Nicólaos G. Alexópoulos, (S'68–M'69–SM'82–F'87) was born in Athens, Greece, on April 14, 1942. He received the degree from the Eighth Gymnasium of Athens, Greece, in 1959, and the B.S.E.E., M.S.E.E., and Ph.D. degrees from the University of Michigan, Ann Arbor, in 1965, 1967, and 1968, respectively.

He joined the School of Engineering and Applied Science at the University of California, Los Angeles (UCLA), where he was a member of the faculty of the Electrical Engineering Department from 1969 to 1996. While at UCLA he served as Associate Dean of Faculty Affairs from 1986 to 1987 and Chair of the Electrical Engineering Department from 1987 to 1992. Since January 1997 he has been a Professor of the Electrical and Computer Engineering Department at the University of California, Irvine, where he also serves as the Dean of the School of Engineering. He has served over the years as a Consultant to a variety of U.S. and foreign corporations and the U.S. Government. In addition, he has been on the editiorial board of various professional journals and, more recently, he served as Editor-in-Chief of *Electromagnetics*. He is the author of over 250 refereed jounal and conference proceedings papers. His recent research activities have focused on the modeling and design of three-dimensional integrated circuits and printed antennas in multilayered materials, wireless communication antennas and systems, interconnect problems in complex networks, novel materials and smart structures in low-observable systems, and computational methods.

Dr. Alexopulos was corecipient of the IEEE (Institute of Electrical and Electronic Engineers) S. E. Schelkunoff Prize Best Paper Award in 1985 and 1998.